

We are IntechOpen, the world's leading publisher of Open Access books Built by scientists, for scientists

6,900

Open access books available

185,000

International authors and editors

200M

Downloads

Our authors are among the

154

Countries delivered to

TOP 1%

most cited scientists

12.2%

Contributors from top 500 universities



WEB OF SCIENCE™

Selection of our books indexed in the Book Citation Index
in Web of Science™ Core Collection (BKCI)

Interested in publishing with us?
Contact book.department@intechopen.com

Numbers displayed above are based on latest data collected.
For more information visit www.intechopen.com



MoS₂ Thin Films for Photo-Voltaic Applications

*Manuel Ramos, John Nogan, Manuela Ortíz-Díaz,
José L Enriquez-Carrejo, Claudia A Rodríguez-González,
José Mireles-Jr-García, Roberto Carlos Ambrosio-Lazáro,
Carlos Ornelas, Abel Hurtado-Macias, Torben Boll,
Delphine Chassaing and Martin Heilmaier*

Abstract

The low dimensional chalcogenide materials with high band gap of ~1.8 eV, specially molybdenum di-sulfide (MoS₂), have been brought much attention in the material science community for their usage as semiconducting materials to fabricate low scaled electronic devices with high throughput and reliability, this includes also photovoltaic applications. In this chapter, experimental data for MoS₂ material towards developing the next generation of high-efficiency solar cells is presented, which includes fabrication of ~100 nm homogeneous thin film over silicon di-oxide (SiO₂) by using radio frequency sputtering at 275 W at high vacuum ~10⁻⁹ from commercial MoS₂ 99.9% purity target. The films were studied by means of scanning and transmission electron microscopy with energy disperse spectroscopy, grazing incident low angle x-ray scattering, Raman spectroscopy, atomic force microscopy, atom probe tomography, electrical transport using four-point probe resistivity measurement as well mechanical properties utilizing nano-indentation with continuous stiffness mode (CSM) approach. The experimental results indicate a vertical growth direction at (101)-MoS₂ crystallites with stacking values of 7-laminates along the (002)-basal plane; principal Raman vibrations at E_{2g}^1 at 378 cm⁻¹ and A_g^1 at 407 cm⁻¹. The hardness and elastic modulus values of $H = 10.5 \pm 0.1$ GPa and $E = 136 \pm 2$ GPa were estimated by CSM method from 0 to 90 nm of indenter penetration; as well transport measurements from -3.5 V to +3.5 V indicating linear Ohmic behavior.

Keywords: thin film, electron microscopy, MoS₂ sputtering, harness, elastic modulus, x-ray diffraction, electrical transport, focus ion-beam, atom probe tomography

1. Introduction

Layered chalcogenide materials have been of high relevance since almost 40 years for their diverse applications such as tribology [1], chemical catalysis [2] and nowadays as semiconductors towards development of high-throughput and energy efficient transistors and devices [3, 4]. MoS₂ is a two-dimensional material

with a band gap ranging between 0.9 and 1.8 eV as calculated theoretically by first principles methods and as measured experimentally by Kam & Parkinson using photo-spectroscopy as a function of crystal orientation [5, 6]. The crystal structure of MoS₂ is hexagonal with space group R3m ($a = b = 3.16 \text{ \AA}$ and $c = 18.41 \text{ \AA}$), having *d*-bonded layers of S-Mo-S along a-b plane which are stacked along c-axis by weak Van der Waals forces with 6.2 Å of separation within layers [7]. The crystal structure was studied using electron microscopy techniques as described by Chianelli et al. who were able to observe its layered structure [8]. However, electron beam dosage during electron microscopy studies plays an important role to avoid any structural damage as described by Ponce et al. when using TEM technique who concluded high-resolution imaging at operational voltages near ~80 kV [9] to be possible. By *in-situ* TEM, Helveg et al. were able to synthesize small clusters of MoS₂ from molybdenum oxide and hydrogen sulfide gases at beam radiation dosage of $100 \text{ e}^-/\text{\AA}^2\text{s}$ [10]. The mechanical properties were studied by Casillas et al. achieving an atomistic observation of a resilient nature on MoS₂ laminates at 8GPa of external applied pressure and its mechanical recovery during *in-situ* AFM on TEM sample holder [11]. Applying atomic force microscopy (AFM), Bertolazzi et al. determined a Young modulus values of $270\text{GPa} \pm 100\text{GPa}$ and fracture strength of 16~30GPa in MoS₂ layers as suspended in patterned silicon wafers [12, 14], and Castellanos-Gomez et al. estimated an average Young modulus $E = 330\text{GPa}$ in suspended MoS₂ sheets over patterned silicon wafer [13]. The mechanical properties were studied by density functional theory and molecular dynamics, Jiang et al. calculated a theoretical Poisson's ratio value of $\nu = 0.29$ applying Stillinger-Weber potential [15]. The reactive empirical bond-order (REBO) potential was used by Li et al. to understand structural effects at chemical bonding within S-Mo-S layers, their findings indicate induced vacancies on the basal plane can influence Poisson's ratio values [16]. The atom probe tomography enables the chemical understanding with three-dimensional spatial resolution and was applied to determine dopants, contamination and ionic distribution within semiconducting matrix [17], Singh et al. used APT technique to determine distribution of Ti over MoS₂ matrix [18]. Regarding electrical transport, Lia et al. [4] and Samuel et al. [38] performed transport electrical measurements encountering a linear ohmic behavior in MoS₂. This chapter covers mechanical, electrical and microstructure characterization by electron microscopy, low angle x-ray, atom probe tomography and CSM-nanoindentation to obtain information about crystal growth, elastic modulus (E), hardness (H) and electrical transport on MoS₂ films.

2. Experimental methods and results

2.1 RF sputtering

The Molybdenum di-Sulfide (MoS₂) films were fabricated with a high vacuum Kurt J. Lesker© PVD 75 machine; applying RF-sputtering at a rate of $2.26 \text{ \AA}/\text{sec}$ at 275 W of plasma power over 4"-diameter silicon oxide (SiO₂) wafers. The films were deposit from commercial MoS₂ 99.9% targets (Kurt J. Lesker). By using dwell time of 300 seconds a film thickness value of ~100 nm was achieved as indicated by profilometry measurements, **Figure 1E**.

2.2 Scanning electron microscopy

The film morphology and crystallographic structure were investigated using scanning and high-resolution transmission electron microscopy (SEM, TEM). SEM

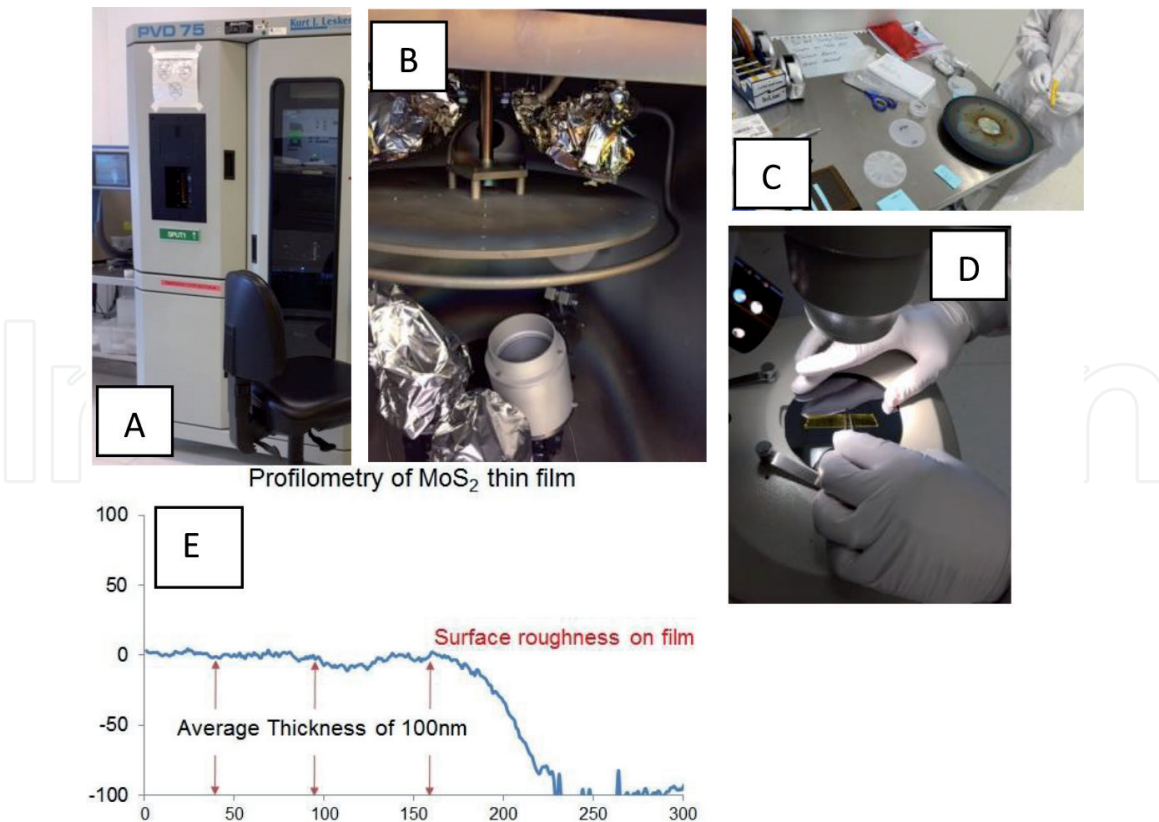


Figure 1. Collage of photographic images taken at the Center for Integration of nanotechnologies-Albuquerque, NM. (A) High-vacuum sputtering device, overview. (B) RF-magnetrons with MoS₂ target mounted. (C) Table showing the sample mounting. (D) Optical inspection of the films. (E) Profilometer measurements indicating the film thickness ~ 100 nm for 300 seconds at a rate of 2.26 Å/sec.

was performed in a Hitachi® SU5500 unit, equipped with Energy-dispersive X-ray spectroscopy (EDS) unit and operated at 30 kV with 8A of current to avoid surface damage on the film. Observations indicate a high-degree of porosity and vertically aligned MoS₂ film matrix, as presented in **Figure 2A–C** which is in agreement with Kong et al. [18]. EDS analysis reveals the two main signals that correspond to Sulfur-K_α and Molybdenum-L_α at 2.4 keV, as presented in **Figure 2E**, in agreement with Lince & Fleischauer [20].

2.3 Transmission electron microscopy and atom probe tomography

The microstructure of MoS₂ thin matrix was also studied using *Scanning Electron Transmission Microscopy* (STEM) using a Cs-corrected 2200-JEOL, with STEM unit, equipped with a high-angle annular dark-field (HAADF) detector, X-Twin lenses and CCD camera. A lamella was prepared using Focus-Ion Beam model JEOL JEM 9320 at 30 kV and 25 mA, MoS₂ film surface coated with gold and gallium. *Atom Probe Tomography* (APT) was performed on Cameca® LEAP 4000X high-resolution system in laser pulse mode (wavelength ~355 nm), measurements were taken at 60 K with evaporation rate of 0.5 and laser frequency of 100 kHz, laser beam was set to 70pJ/V, all data was reconstructed using IVAS© 3.6.10a package. The samples were prepared using focus ion beam FEI Strata dual-beam instrument coupled with micromanipulator Oxford® Omniprobe® 200 by lift-out method as described by Szász et al. [21]. MoS₂ film surface was protected using platinum layer, and cuts were done at 30 kV at 260pA gun power. Using both techniques, it was possible to determine chemical composition, and spatial resolution of S-Mo-S distribution along film matrix, stacking and orientation, as presented in **Figure 3**. In the image the top part corresponds to MoS₂ and uppermost bright layer is due to gold gallium coating.

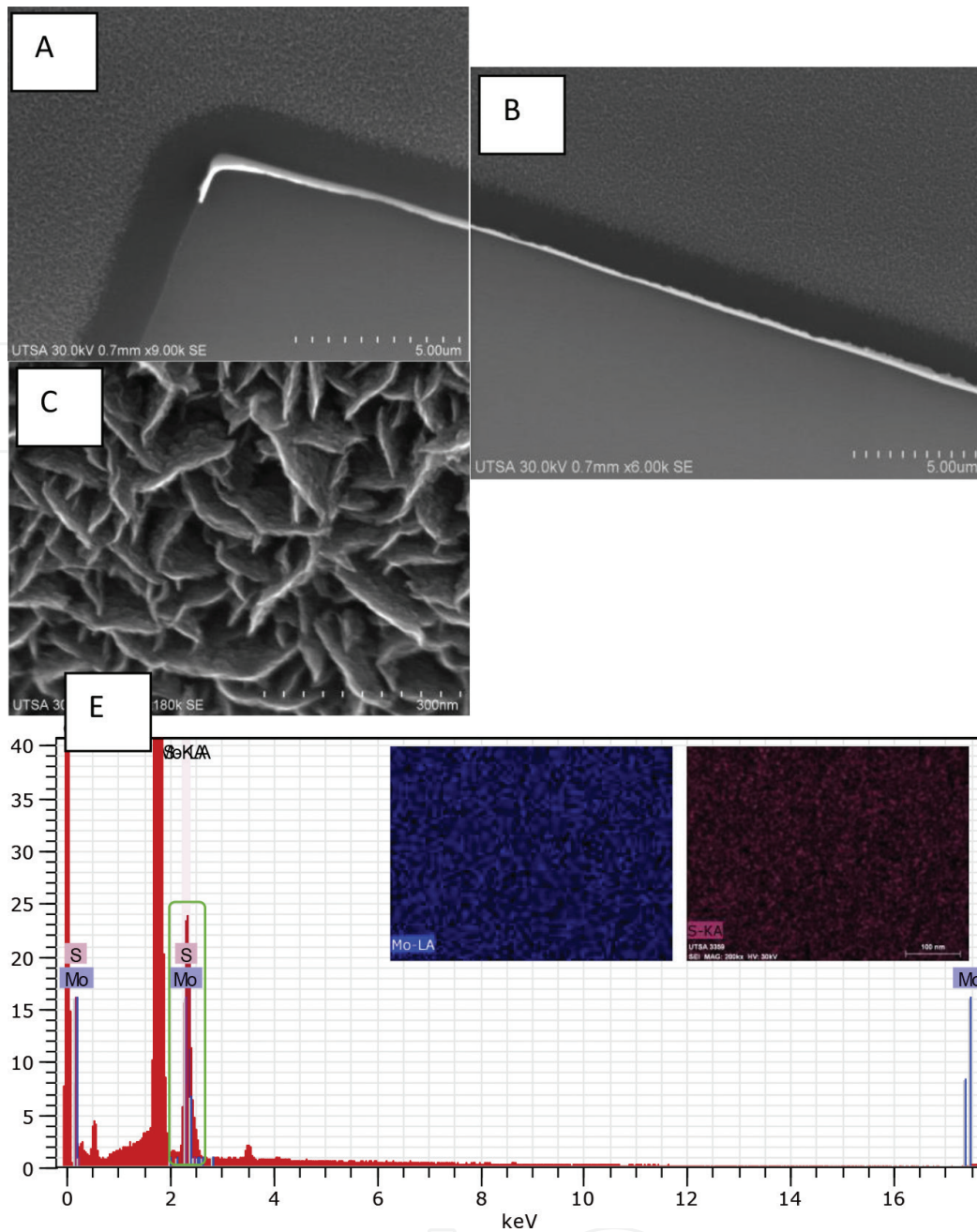


Figure 2. (A, B) Scanning electron micrograph of MoS₂ film matrix at magnification of 6000x. (C) SEM image able to observe laminates vertically aligned at magnification of 200,000x. (E) Energy disperse spectrum from surface to MoS₂ film matrix to determine chemical composition.

The atom probe tomography (APT) is a technique used to understand in a three-dimensional reconstruction with high-spatial resolution the chemical distribution and composition as indicated by Kelly & Miller [17]. A sample is placed in the main APT chamber to undergo an ionizing evaporation process at a high electric field triggered by a laser pulse; the potential energy of an atom at the sample surface, as caused by the applied voltage on the sample neV , is converted into kinetic energy $\sim 1/2mv^2$ in the vicinity of the tip. This relationship, in order to understand the mass-to-charge-state ratio m/n of evaporated ions, is given by Eq. (1); with n as number of electrons removed from the ion, e electron charge ($-1.62 \times 10^{-19}C$), V total applied voltage, m is atomic mass and speed of atoms are given by conventional $v = d/t$, which is with good approximation constant, distance d and lastly t is the time of flight, as described by the schematic drawing taken from Kelly and Larson [23]. Short laser pulses (<1 ns) are used for APT and can field evaporated for almost any material regardless of its electrical conductivity as described by Kellogg et al. [24].

$$\frac{m}{n} = \frac{2e}{d^2} (V_{dc}) t^2 \quad (1)$$

Nowadays, usage of APT to survey spatial distribution of atomistic species in semiconducting devices like n-doped metal-oxide field effect transistors [25] and Singh et al. applied with high success to titanium-MoS₂ and strontium oxide-MoS₂ films [18]. In this case, APT measurements were performed to understand the spatial distribution of MoS₂ film matrix. **Figure 4** illustrates the preparation of APT samples using a FIB (**Figures 5–9**).

2.4 Raman spectroscopy

The Raman spectroscopy was obtained using Alpha 300RA system equipped with a 532 nm Nd-YAG laser and a 100X 0.9 NA objective. The laser power was varied to avoid surface damage; with no additional sample preparation during study. Modes of vibration at E_{2g}¹ = 378 cm⁻¹ and A_g¹ = 407 cm⁻¹ are indicators of sulfur vibrations caused by dangling bonds on S-Mo-S chemical structure as indicated schematically **Figure 10** (insets).

2.5 Grazing incidence X-ray diffraction (GIXD)

X-ray diffraction was collected using a Panalytical X-Pert system with source of Cu_{Kα} λ = 1.41 Å radiation. The grazing incidence angle was fixed at 0.5° with 20° < θ < 80° and step size of 0.02° with a graphite flat crystal monochromator, described by Liu et al. while characterizing same layers of MoS₂ [26] and presented in **Figure 11**.

2.6 Nanoscale mechanical properties

The nanoscale mechanical properties were evaluated to obtain Elastic modulus (*E*) and Hardness (*H*) of MoS₂ thin films; this was possible using an Agilent nanoindenter model G200 coupled with a DCM II head instrument and Berkovich diamond indenter tip radius of 20 ± 5 nm, penetration depth limit of 400 nm, strain rate of 0.05 s⁻¹, and harmonic displacement and frequency of 1 nm and 75 Hz, Poisson's coefficient of ν = 0.22. The equipment was calibrated using a standard

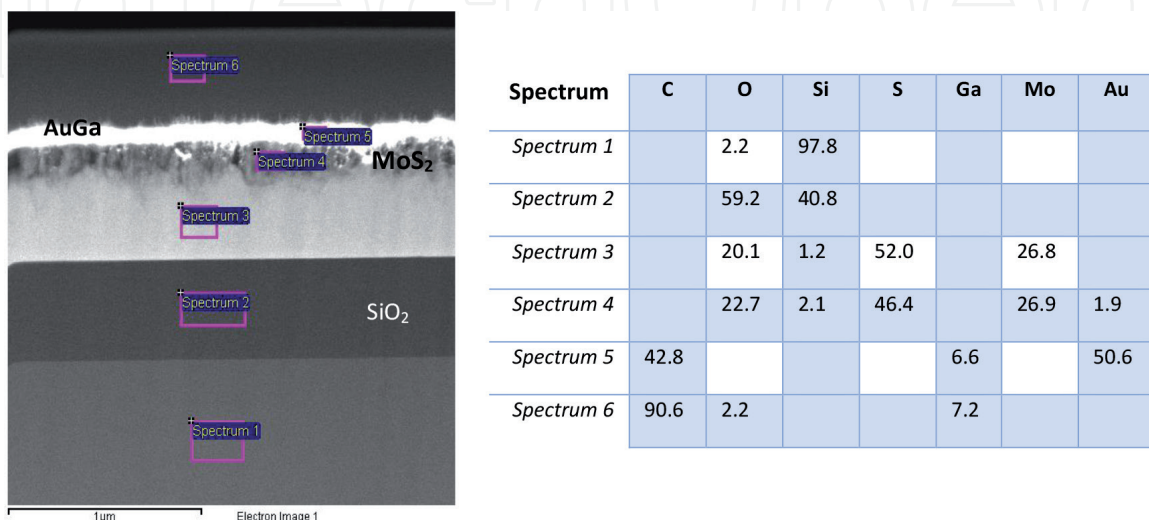
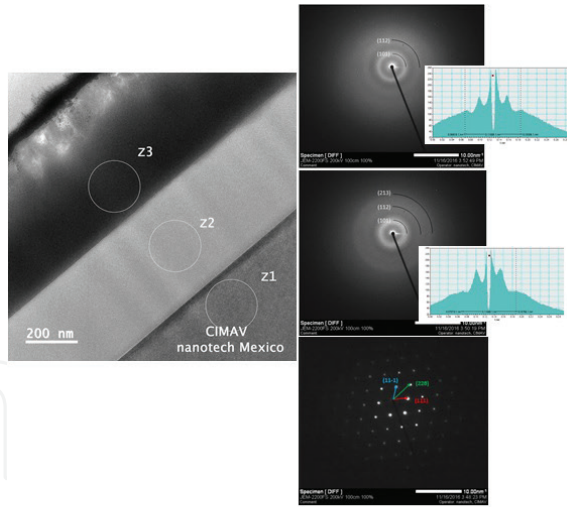


Figure 3. **Left:** Cross-sectional view of MoS₂ film on TEM. **Right:** Chemical composition at locations as indicated in the image (violet squares), obtained during TEM observations.



Zone	d-Theoretical (Å)	d-Experimental (Å)	Crystallographic Planes	Theoretical Angles	Experimental Angles
Z1	3.138	3.124	(111)	--	---
Z1	1.92	1.93	(220)	35.26	34.61
Z1	3.138	3.198	(11-1)	70.53	70.5
Z2	3.35	3.49	(101)	--	---
Z2	1.81	1.71	(112)		
Z2	1.20	1.2	(213)	--	---
Z3	3.35	3.452	(101)	--	---
Z3	1.81	1.718	(112)	--	---

Figure 4. **Left:** Scanning transmission electron micrograph of transversal section of MoS₂ film. **Right:** Selected area diffraction patterns for three different sites as indicated by red circles, the top part corresponds to textural MoS₂ matrix. Table indicates principal with (101) and (112) for MoS₂ in agreement with obtained by GDRX.

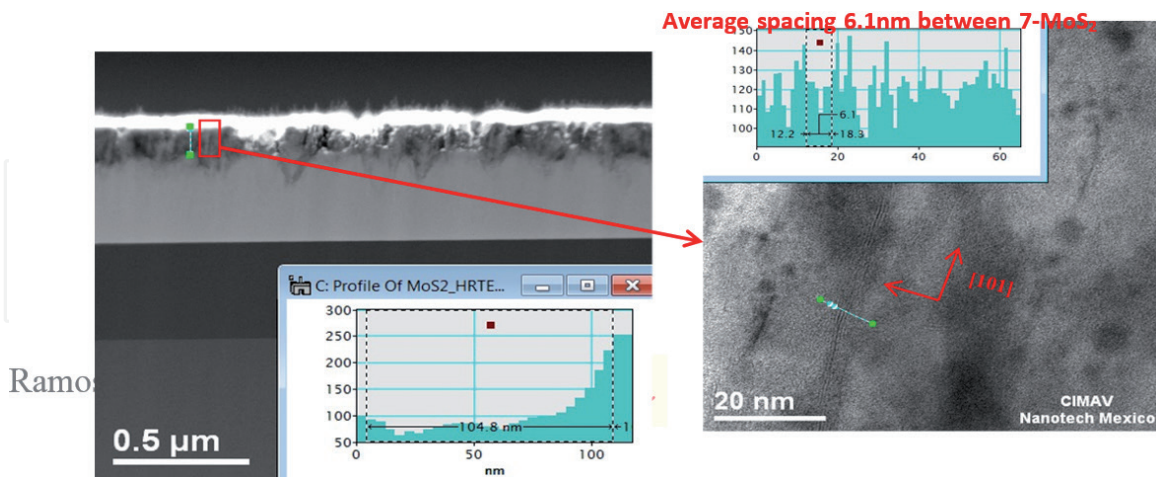


Figure 5. High-resolution STEM image showing a vertical growth of MoS₂ crystallites as confirmed by 0.62 nm interlayer distance in (002) basal plane, in agreement. Image taken with rights and permissions from IOP-surf. Topogr.: Metrol. Prop. © Ramos et al. [22].

fused silica sample, under test parameters of $C_0 = 24.06$, $C_1 = -184.31$, $C_2 = 6532.04$, $C_3 = -25482.45$, and $C_5 = 19015.30$ as constant area of contact for continuous stiffness method (CSM) as described in detail by Li et al. [27]. All data was recorded by AFM Nano Vision© system attached to the nanoindenter system. The estimated values for hardness (H) and elastic modulus (E) were calculated using Eq. (2) to

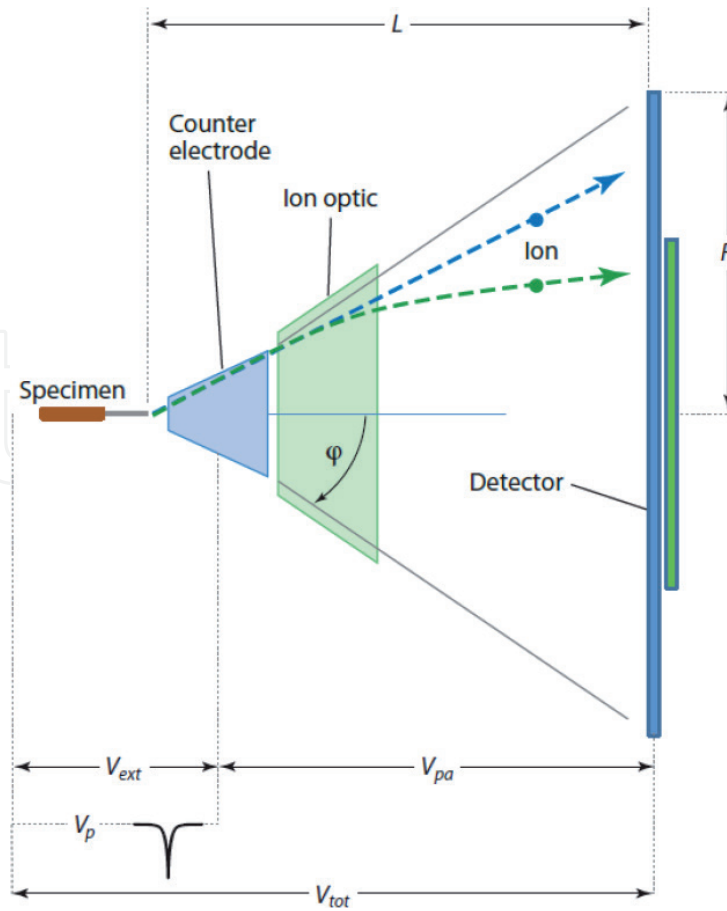


Figure 6.
 Schematic drawing of APT (taken from [23]).

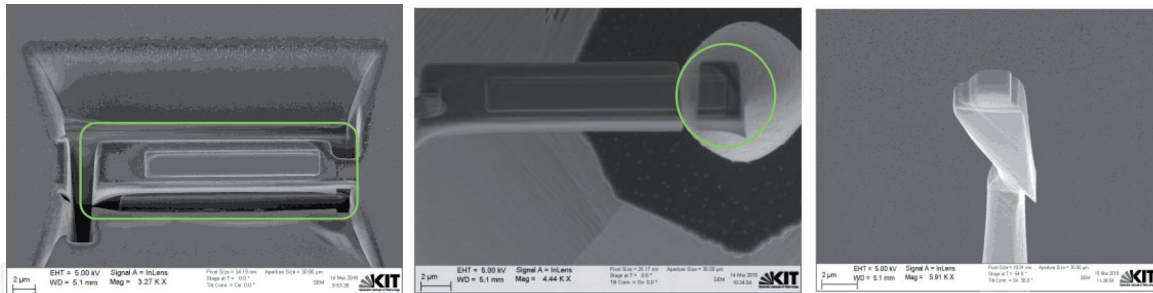


Figure 7.
 Scanning electron images taken during lift-out procedure to prepare a needle for atom probe tomography in MoS₂ thin film (green square and circles are the areas of interest and cut using Ga ions and Omiprobe® micromanipulators), as discussed by Szász et al. [21].

determine stiffness S , when comparing to silicon substrates (001) surface termination and applying a continuous stiffness method as described extensively by Pharr et al. [28].

$$S = \left| \frac{1}{\frac{F_0}{Z_0} \cos \varphi - (K_s - m \omega^2)} - \frac{1}{K_f} \right|^{-1} \quad (2)$$

In Eq. (2), ω is the excitation frequency, (Z_0) displacement amplitude, (φ) phase angle, and (F_0) is the excitation amplitude, all those values can be obtained if the machine parameters load-frame stiffness K_f and stiffness of springs (K_s) as well the mass m are known input values during nanoindentation test. The coating hardness of film H_f can be estimated using a work indentation model described by

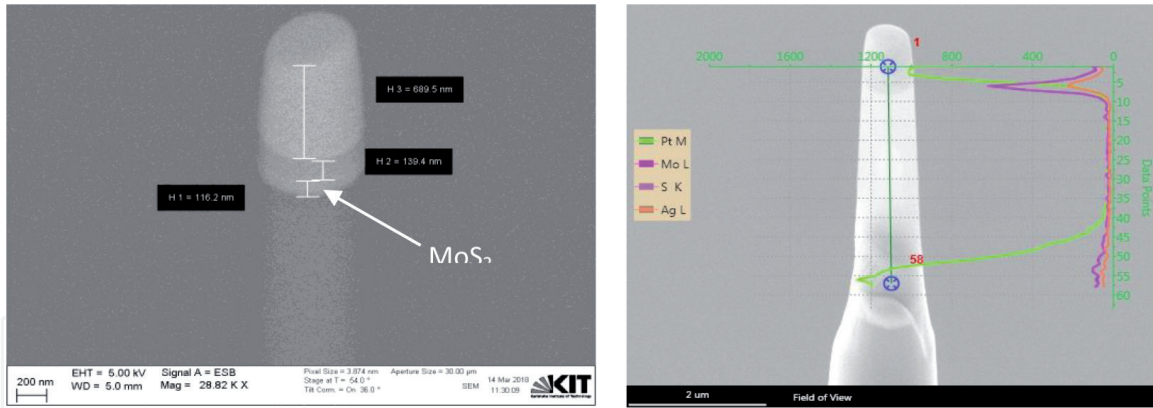


Figure 8. Scanning electron images and line scan EDS to map chemical composition on the needle; molybdenum and sulfur atoms were detected over MoS₂ section (~ 110 nm).

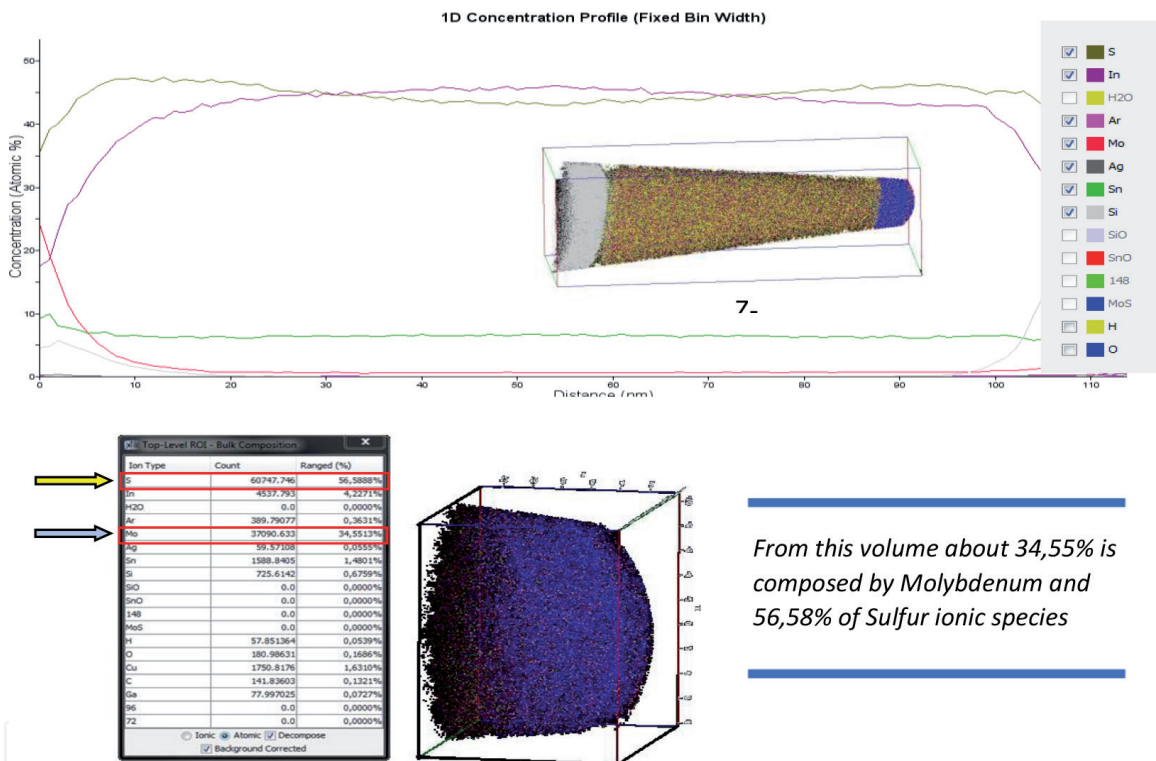


Figure 9. Top: Atomic concentration profile from atom probe tomography for the MoS₂ thin film (~110 nm). Bottom: Portion of APT needle where corresponding to MoS₂ highest concentration as shown on ions table on left (yellow and blue arrows), in agreement with Singh et al. [18].

From this volume about 34,55% is composed by Molybdenum and 56,58% of Sulfur ionic species

Eq. (3), having H_c as composed film/substrate hardness; H_s and H_f as substrate and film hardness, the constant k represents a fitting parameter determined experimentally from the variation of H_c with relative indentation depth ($\beta = H_c/t$).

$$H_c = H_s + \frac{H_f - H_s}{1 + k\beta^2} \quad (3)$$

The elastic modulus E can be estimated using Eq. (4); having E_{eff} as effective reduced elastic modulus of the system in array film/substrate, contact area is determinate by A as function of the penetration depth, ν is the Poisson ratio, t represents film thickness, and α is a parameter which depends on the material and the indenter

geometry, in our case a pyramidal shape, as described by Domínguez-Rios et al. [29] and Hurtado-Macias et al. [30].

$$\frac{1}{E_{\text{eff}}} = \frac{(1 - \nu_f^2)}{E_f} (1 - e^{-at/\sqrt{A}}) + \frac{(1 - \nu_s^2)}{E_s} (e^{-at/\sqrt{A}}) + \frac{(1 - \nu_i^2)}{e_i} \quad (4)$$

By using CSM method, it was possible to estimate elastic modulus and hardness values as follows: Three regions of test are observed in the **Figures 12 and 13**, where region I is hardness values for MoS₂ crystallites with penetration depth of 0–90 nm, having no influence from silicon oxide substrate and a hardness value of $H = 6.0 \pm 0.1$ GPa and elastic modulus of $E = 136 \pm 2$ GPa. The region II, which has a penetration deep of 90–120 nm both values of elastic modulus and hardness are increased, meaning a clear influence by silicon oxide substrate, as confirmed by profilometry a thin film thickness of ~105 nm (both insets of **Figure 1**). The region III with penetration depth of 120–150 nm represents a hardness and elastic modulus of silicon oxide substrate, which are in partial agreement with Malzbender & With [31] to whom performed similar experiment on SiO₂ spin coated with methyltrimethoxysilane.

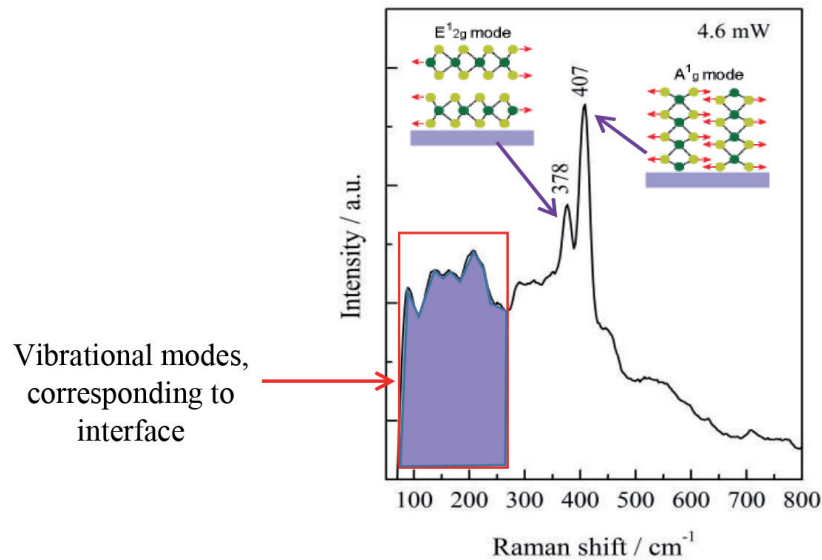


Figure 10. The Raman spectra with two characteristic modes of vibrations at E_{2g}^1 at 378 cm^{-1} and A_g^1 at 407 cm^{-1} , in agreement with Kong et al. [19].

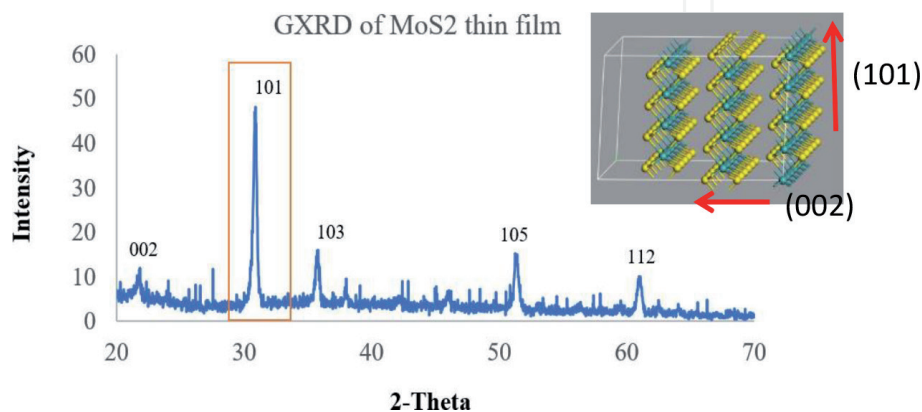


Figure 11. Grazing incidence x-ray diffraction it was possible to observe a dominant (101) reflection at $2\theta \sim 30^\circ$, in agreement with Liu et al. [26] for vertical aligned layers.

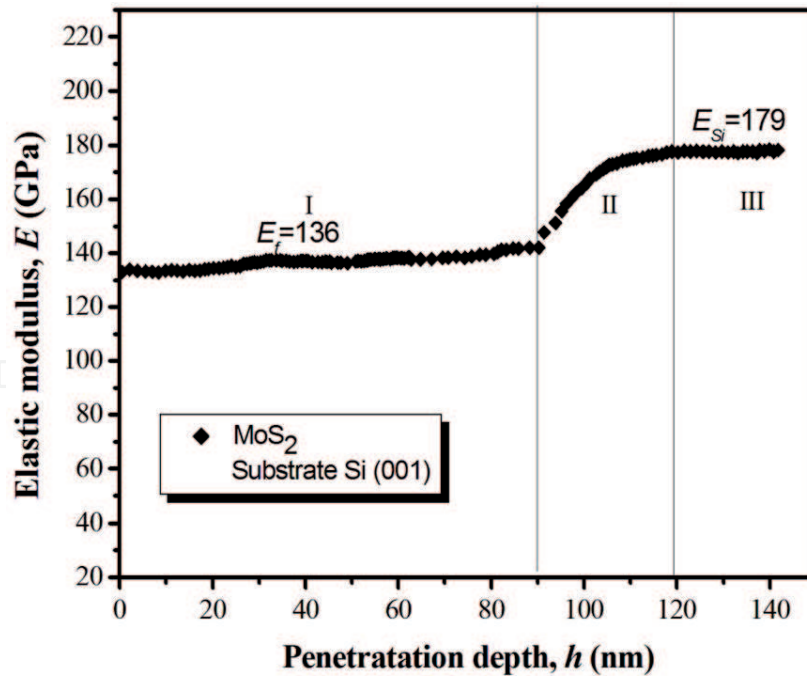


Figure 12.

Nanoindentation curves estimated experimentally using continuous stiffness method (CSM), the curve corresponds to regions I, II, III. In region I the estimated elastic modulus is $E = 136 \pm 2$ GPa corresponds to 0–90 nm of penetration depth, which is indicated to be only for MoS₂ film, in agreement with [28].

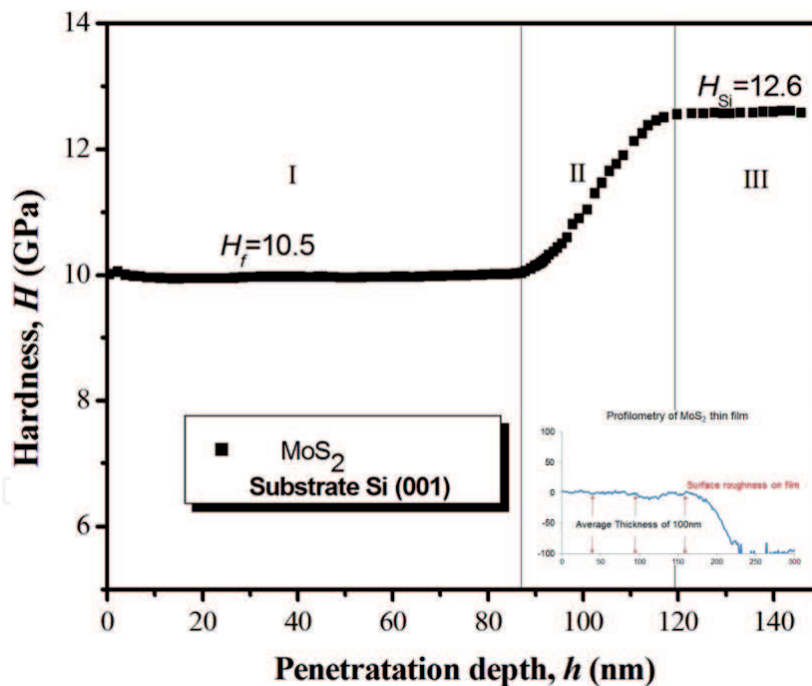


Figure 13.

The region I corresponds to hardness values of $H = 10.5 \pm 0.1$ GPa at 0–90 nm of penetration depth corresponding to MoS₂ layer. The regions II and III on both curves corresponds to mixed stage MoS₂/SiO₂ and SiO₂ substrate reason of an increase on both values are observed, in agreement with [28].

The obtained values for hardness and elastic modulus are smaller estimations when comparing with results as presented by Bertolazzi et al. [12, 14] for single layers of MoS₂; we believe this occurs because of low dimension laminates can be stronger than stacking of MoS₂ crystallites. The applied force was done over (001)-basal plane as suspended on patterned silicon holes [12, 14], and in this case indenter tip can sweep MoS₂ crystallites over surface area. For that reason, our research team proceed to estimate film adherence by using AFM scratching technique in

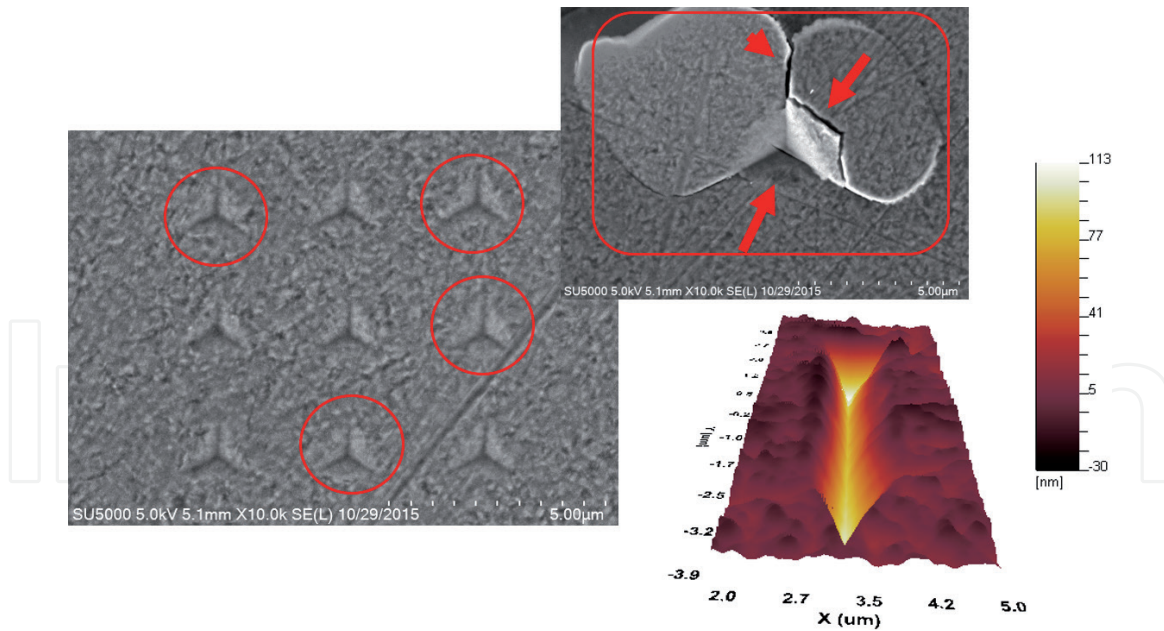


Figure 14. **Left:** Scanning electron micrograph indicating the nine zones of nanoindentation made with diamond indenter tip to estimate the elastic modulus and hardness values on MoS₂ film. **Center:** Scanning electron micrograph showing cracks over triangle shape indentation as indicated by red arrows. **Right:** Atomic force microscope starching zone to estimate a stiffness values of 4.27kN/m over the MoS₂ film.

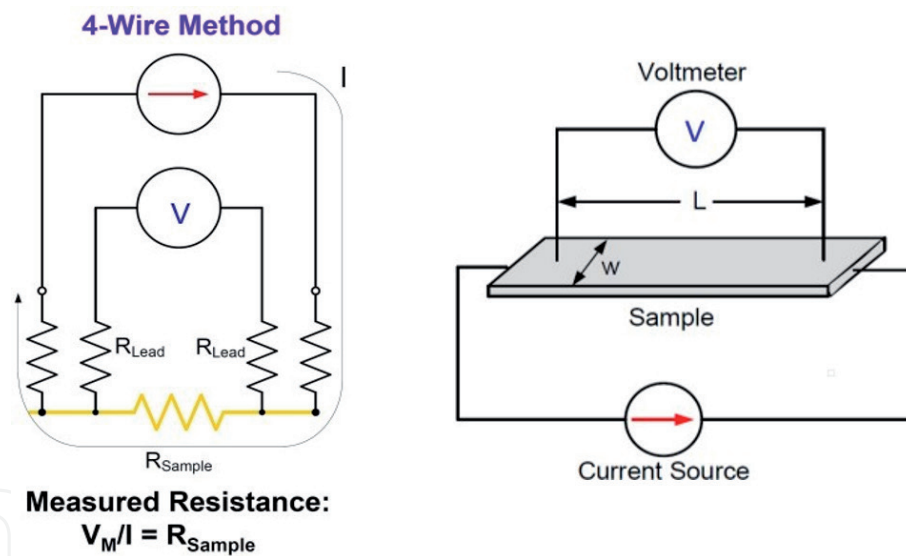


Figure 15. Graphical description of the four-point method implemented for electrical transport in MoS₂ film.

encountering a deformation $0.85 \mu\text{m}^2$ with a residual groove width $1 \mu\text{m}$ (a total groove height 125 nm and pile up height 40 nm), as presented in **Figure 14**, along with indentation sites completed to obtain elastic modulus and hardness values.

2.7 Electrical transport and resistivity

The electrical transport of the MoS₂ film matrix was investigated using four-point probe method as indicated in **Figure 15**, equipped with Keithley 4200-SCS in applied voltage range from -3.5 to 3.5 V . The transport measurements were done at room temperature and by direct contact to the MoS₂ film surface, no especial solder or metallic glue was used. Also, they were completed in the presence of light and dark conditions, the results indicate a linear Ohmic behavior, as presented in

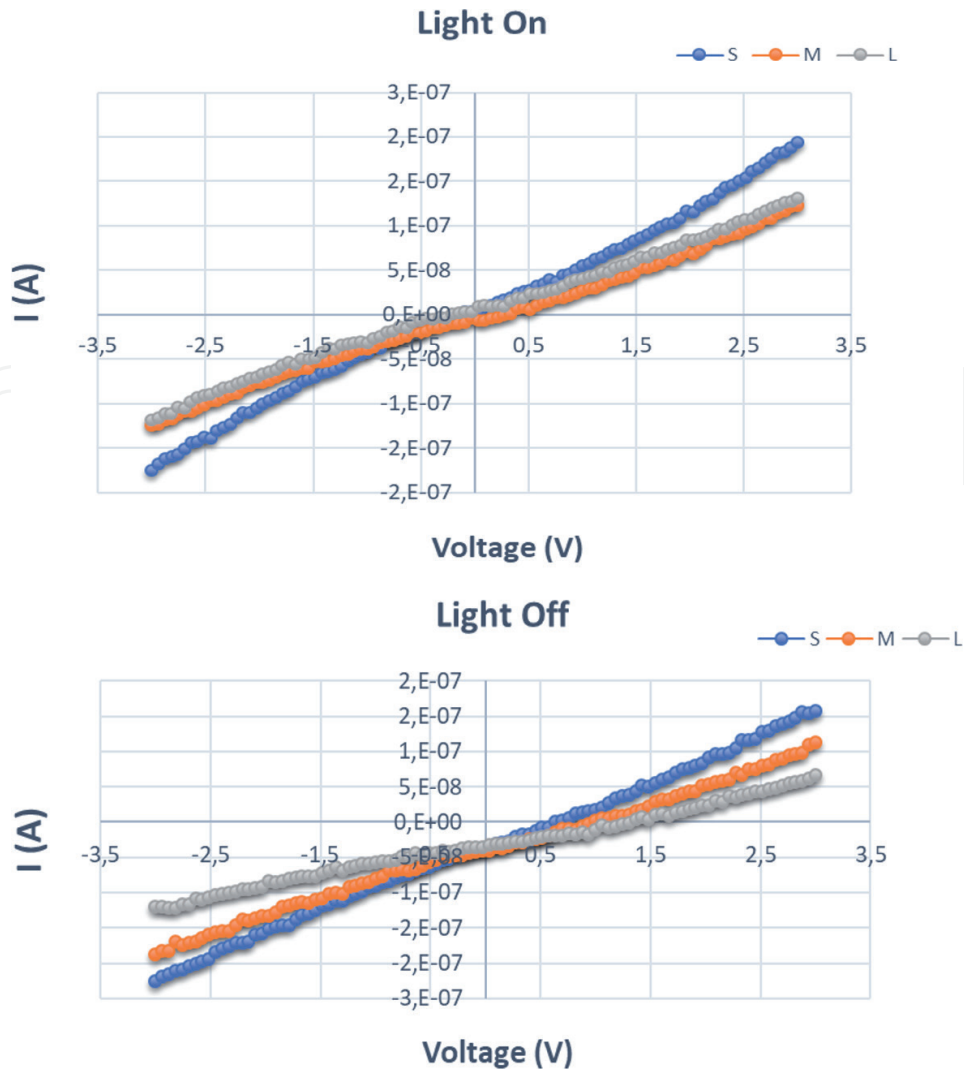


Figure 16.

Top: I-V curves measured in the presence of white light and using four-point method MoS₂ film. *Bottom:* I-V curves measured film in dark-room under otherwise conditions. When comparing both measurements it is possible to observe a change on slope, which is related to resistive values as presented in Figure 17.

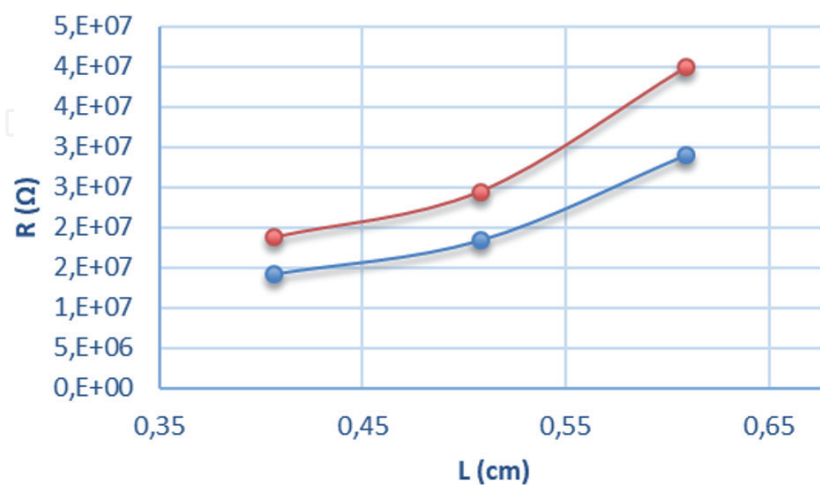


Figure 17.

Resistivity ρ values, calculated from I-V curves measured in the presence of white light and dark environment by using four-point method over MoS₂ film's surface. Red curve corresponds to presence of light shining on surface and blue curve to dark-room conditions.

Figure 16 and resistivity values in Figure 17, from Tables 1 and 2 it was possible to determine values differences when white light is present, some authors refer this as photo-voltaic effect due to its intrinsic semiconductor nature of MoS₂ [2, 32, 33].

Size (m)	Impedance	Resistance	Power	Resistivity (Ω/m)
5×10^{-3}	0.4064	1.41×10^6	0.0381	26.507
10×10^{-3}	0.508	1.83×10^6	0.0381	27.473
15×10^{-3}	0.6096	2.89×10^6	0.0254	24.106

Table 1.
 Values of impedance, resistance, power and resistivity measured without presence of white light.

Size (m)	Impedance	Resistance	Power	Resistivity (Ω/m)
5×10^{-3}	0.4064	1.86×10^6	0.0381	35.047
10×10^{-3}	0.508	2.46×10^6	0.0381	36.605
15×10^{-3}	0.6096	3.92×10^6	0.0254	33.256

Table 2.
 Values of impedance, resistance, power and resistivity measured in presence of white light.

3. Discussion and conclusion

By using radio frequency sputtering techniques at high-vacuum it was possible to fabricate MoS₂ films with thickness of ~100 nm over pristine silicon oxide (SiO₂) wafers. The film surface analysis was carried out using electron microscopy and spectroscopy techniques and results indicate molybdenum di-sulfide had a vertical crystallite growth as shown in **Figures 2C** and **5**. Energy disperse confirms Sulfur-K α (60%) and Molybdenum-L α (40%) at 2.4 keV signal; and Raman spectroscopy modes of vibration at surface corresponding to E_{2g}¹ = 378 cm⁻¹ and A_g¹ = 407 cm⁻¹. From high-resolution STEM it was possible to determine a degree of stacking between 7 layers along (002)-basal plane and to confirm vertical growth in agreement with Kong et al. [19], and APT preliminary measurements indicate a large quantity of sulfur and molybdenum with no grain boundaries or high impurities within film matrix for specific thin film growth using RF-sputtering conditions. From electrical transport measurements, it was possible to determine a linear Ohmic behavior and excitation when external visible light was on and off during four-point probe measurements as indicated by **Figure 16**, the resistivity values 26.5 Ω/m versus 35.0 Ω/m for off and on in external visible light, as possible caused by intrinsic semiconductor nature of MoS₂ in agreement with [2, 32, 33]. The mechanical properties were also investigated as previously reported by Ramos et al. [22] for indenter penetrating film surface 0-90 nm it was possible to estimate hardness of $H = 10.5 \pm 0.1$ GPa and elastic modulus $E = 136 \pm 2$ GPa by the continuous stiffness method [28]. It was concluded that MoS₂ films are a promising semiconducting material candidate for large scale photovoltaic applications, due to low cost and reliable and straight forward approach for homogenous low dimension films and its possible chemical combination with other group VI semiconducting materials as indicated by Najmaei et al. [34, 35] and Matis et al. [36] and Paranjape et al. [37–42].

Acknowledgements

The principal author thanks Universidad Autónoma de Ciudad Juárez for financial support by PIVA-2017 project titled: “Fabricación de plantillas metálico-orgánicas: Una ruta hacia celdas solares más eficientes” and PROFOCIE 2015. The

Laboratorio Nacional de Nanotecnología of Centro de Investigación en Materiales Avanzados (CIMAV-Chihuahua) and ICNAM program of Kleberg Advanced Laboratory Center of University of Texas at San Antonio both for the usage of electron microscopy and characterization equipment and facilities. Part of this work was performed at the Center for Integrated Nanotechnologies, an Office of Science User Facility operated for the U.S. Department of Energy (DOE) Office of Science. Sandia National Laboratories is a multi-program laboratory managed and operated by Sandia Corporation, a wholly owned subsidiary of Lockheed Martin Corporation, for the U.S. Department of Energy's National Nuclear Security Administration under contract DE-AC04-94AL85000. We are grateful to the Karlsruhe Micro and Nano Facility (KNMF) of Karlsruhe Institute of Technology for usage of Atom Probe Tomography and FIB instruments, under proposal 2018-020-022609. To facultad de ciencias de la electronica of Benemerita Universidad Autónoma de Puebla for usage of four-point probe station and laboratory facilities.

Conflict of interest

Authors declare no conflict of interest.

Author details

Manuel Ramos^{1,2*}, John Nogan², Manuela Ortíz-Díaz¹, José L Enriquez-Carrejo¹, Claudia A Rodriguez-González¹, José Mireles-Jr-García¹, Roberto Carlos Ambrosio-Lazáro⁴, Carlos Ornelas³, Abel Hurtado-Macias³, Torben Boll⁵, Delphine Chassaing⁵ and Martin Heilmaier⁵

¹ Departamento de Física y Matemáticas, Instituto de Ingeniería y Tecnología, Universidad Autónoma de Cd. Juárez, Chihuahua, CP, Mexico

² Center for Integrated Nanotechnologies, Albuquerque, NM, USA

³ Laboratorio Nacional de Nanotecnología, Centro de Investigación en Materiales Avanzados S.C., Chihuahua, CP, México

⁴ Facultad de Ciencias de la Electrónica, Benemérita Universidad Autónoma de Puebla, Ciudad de Puebla, Estado de Puebla, CP, México

⁵ Institut für Angewandte Materialien-Werkstoffkunde (IAM-WK), Karlsruher Institut für Technologie, Karlsruhe, Germany

*Address all correspondence to: manuel.ramos@uacj.mx

IntechOpen

© 2019 The Author(s). Licensee IntechOpen. This chapter is distributed under the terms of the Creative Commons Attribution License (<http://creativecommons.org/licenses/by/3.0>), which permits unrestricted use, distribution, and reproduction in any medium, provided the original work is properly cited. 

References

- [1] Chianelli RR, Berhault G, Torres B. Unsupported transition metal sulfide catalysts: 100 years of science and application. *Catalysis Today*. 2009;**147**:275-286
- [2] Villareal A et al. Importance of the sulfidation step in the preparation of highly active NiMo/SiO₂/Al₂O₃ hydrodesulfurization catalysts. *Catalysis Today*. 2015;**250**:60-65
- [3] Olivas A, Alonso G, Fuentes S. The catalytic activity of Ni/W bimetallic sulfide nanostructured catalysts in the hydrodesulfurization of dibenzothiophene. *Topics in Catalysis*. 2006;**39**:175-179
- [4] Siadati MH, Alonso G, Torres B, Chianelli R. Open flow hot isostatic pressing assisted synthesis of unsupported MoS₂ catalysts. *Applied Catalysis A*. 2006;**305**:160-168
- [5] Li W, Jun-fang C, HeQinyu WT. Electronic and elastic properties of MoS₂. *Physica B*. 2010;**405**:2498-2502
- [6] Ramírez J, Macías G, Cedeño L, Gutiérrez-Alejandro A, Cuevas R, Castillo P. The role of titania in supported Mo, CoMo, NiMo, and NiW hydrodesulfurization catalysts: analysis of past and new evidences. *Catalysis Today*. 2004;**98**(1-2):19-30
- [7] Stanislaus A, Marafi A, Rana MS. Recent advances in the science and technology of ultra low sulfur diesel (ULSD) production. *Catalysis Today*. 2010;**153**:1-68
- [8] Morales-Ortuño JC, Ortega-Domínguez RA, Hernández-Hipólito O, Bokhimi X, Klimova TE. HDS performance of NiMo catalysts supported on nanostructured materials containing titania. *Catalysis Today*. 2016;**271**:127-139
- [9] Gates BC et al. Catalysts for emerging energy applications. *MRS Bulletin*. 2008;**33**:429-435
- [10] Farragher AL, Cossee P. Proceedings of the 5th International Congress on Catalysis, North-Holland, Amsterdam; Vol. 1301. 1973
- [11] Hagenbach G, Courty P, Delmon B. Physicochemical investigations and catalytic activity measurements on crystallized molybdenum sulfide-cobalt sulfide mixed catalysts. *Journal of Catalysis*. 1973;**31**:264-273
- [12] Candia R et al. Proceedings of the 8th International Congress on Catalysis. Frankfurt-an-Main: Dechema; 1984;**2**:375
- [13] Daage MM, Chianelli RR. Structure-function relations in molybdenum sulfide catalysts: The "Rim-Edge" model. *Journal of Catalysis*. 1994;**149**:414-427
- [14] Perdew JP, Burke K, Ernzerhof M. Generalized Gradient Approximation Made Simple. *Physical Review Letters*. 1996;**77**:3865
- [15] Hammer B, Hansen LB, Nørskov K. Improved adsorption energetics within density-functional theory using revised Perdew-Burke-Ernzerhof functionals. *Physical Review B*. 1999;**59**:7413
- [16] Lauritsen JV et al. Location and coordination of promoter atoms in Co- and Ni-promoted MoS₂-based hydrotreating catalysts. *Journal of Catalysis*. 2007;**249**:220-233
- [17] Remškar M, Viršek M, Mrzel A. The MoS₂ nanotube hybrids. *Applied Physics Letters*. 2009;**95**:133122
- [18] Camacho-Bragado GA, Elechiguerra JL, Yacaman M. Characterization

of low dimensional molybdenum sulfide nanostructures. *Materials Characterization*. 2008;**59**:204-212

[19] Blanco E, Afanasiev P, Berhault G, Uzio D, Loridant S. Resonance Raman spectroscopy as a probe of the crystallite size of MoS₂ nanoparticles. *Comptes Rendus Chimie*. 2016;**19**:1310-1314

[20] Ramos MA et al. Spherical MoS₂ micro particles and their surface dispersion due to addition of cobalt promoters. *Revista Mexicana de Física*. 2011;**57**:220-223

[21] Ramos MA, Berhault G, Ferrer DA, Torres B, Chianelli RR. HRTEM and molecular modeling of the MoS₂-Co₉S₈ interface: understanding the promotion effect in bulk HDS catalysts. *Catalysis Science & Technology*. 2012;**2**:164-178

[22] Hansen LP, Johnson E, Brorson M, Helveg S. Growth mechanism for single- and multi-layer MoS₂ nanocrystals. *Journal of Physical Chemistry C*. 2014;**118**:22768-22773

[23] Casillas G et al. Elasticity of MoS₂ sheets by mechanical deformation observed by in situ electron microscopy. *Journal of Physical Chemistry C*. 2015;**119**:710-715

[24] Ramos M et al. In-situ HRTEM study of the reactive carbide phase of Co/MoS₂ catalyst. *Ultramicroscopy*. 2013;**127**:64-69

[25] Midgley PA, Dunin-Borkowski RE. Electron tomography and holography in materials science. *Nature Materials*. 2009;**8**:271-280

[26] Ziese U, de Jong KP, Koster AJ. Electron tomography: a tool for 3D structural probing of heterogeneous catalysts at the nanometer scale. *Applied Catalysis A: General*. 2004;**260**:71-74

[27] Arslan I, Marquis EA, Homer M, Hekmaty MA, Bartelt NC. Towards

better 3-D reconstructions by combining electron tomography and atom-probe tomography. *Ultramicroscopy*. 2008;**108**:1579-1585

[28] Ma L, Chen W-X, Xu L-M, Zhou X-P, Jin B. One-pot hydrothermal synthesis of MoS₂ nanosheets/C hybrid microspheres. *Ceramics International*. 2012;**38**:229-234

[29] Sanders T, Prange M, Akatay C, Binev P. Physically motivated global alignment method for electron tomography. *Advanced Structural and Chemical Imaging*. 2015;**1**:11-11

[30] Sanders T. Discrete iterative partial segmentation technique (DIPS) for tomographic reconstruction. *IEEE Transactions on Computational Imaging*. 2016;**2**:71-82

[31] Coelho A. TOPAS-academic V4. Vol. 1. Australia: Coelho Software, Brisbane; 2007

[32] Magini M et al. Programme en FORTRAN IV pour l'analyse des données expérimentales relatives à la diffusion des rayons X par des substances liquides, amorphes et microcristallisées. *Journal of Applied Crystallography*. 1972;**5**:14

[33] Niemantsverdriet JW. et al. Catalysis—Biocatalytic Processes Encyclopedia of Life Support Systems (EOLSS). 2007

[34] Ertl G. Oscillatory catalytic reactions at single-crystal surfaces. *Advances in Catalysis*. 1990;**37**:213-277

[35] Imbihl R, Ertl G. Oscillatory Kinetics in Heterogeneous Catalysis. *Chemical Reviews*. 1995;**95**:697-733

[36] Wang S et al. A new molybdenum nitride catalyst with rhombohedral MoS₂ structure for hydrogenation applications. *Journal of the American Chemical Society*. 2015;**137**:4815-4822

[37] Galindo-Hernández F, Domínguez JM, Portales B. Structural and textural properties of Fe₂O₃/γ-Al₂O₃ catalysts and their importance in the catalytic reforming of CH₄ with H₂S for hydrogen production. *Journal of Power Sources*. 2015;287:13-24

[38] Samuel J, Ottolenghi M, Avnir D. Diffusion limited reactions at solid-liquid interfaces: Effects of surface geometry. *Journal of Physical Chemistry*. 1991;95:1890-1895

[39] Avnir D et al. Fractal analysis of size effects and surface morphology effects in catalysis and electrocatalysis. *Chaos*. 1991;1:397-410

[40] Magini M et al. Programme en FORTRAN IV pour l'analyse des données expérimentales relatives à la diffusion des rayons X par des substances liquides, amorphes et microcristallisées. *Journal of Applied Crystallography*. 1972;5:14

[41] Seri-Levy A, Avnir D. Effects of heterogeneous surface geometry on adsorption. *Langmuir*. 1993;9:3067-3076

[42] Neimark AV. Calculating Surface Fractal Dimensions of Adsorbents. *Adsorption Science Technology*. 1991;7:210-219